CrossMark

Shock Waves in Supernova Ejecta

J.C. Raymond[1]

Abstract Astrophysical shock waves are a major mechanism for dissipating energy, and by heating and ionizing the gas they produce emission spectra that provide valuable diagnostics for the shock parameters, for the physics of collisionless shocks, and for the composition of the shocked material. Shocks in SN ejecta in which H and He have been burned to heavier elements behave differently than shocks in ordinary astrophysical gas because of their very large radiative cooling rates. In particular, extreme departures from thermal equilibrium among ions and electrons and from ionization equilibrium may arise. This paper discusses the consequences of the enhanced metal abundances for the structure and emission spectra of those shocks.

1 Introduction

Most of the shock waves familiar to astrophysicists sweep up material of normal astrophysical abundances, which is to say mostly H and He with 0.1% by number of heavier elements. The material in supernova ejecta can be much different, however. CNO processing can eliminate the hydrogen, but if most of the gas is helium the basic shock physics will not be greatly affected. On the other hand, if both H and He are burned to heavier elements, the behavior and appearance of the shock will be drastically altered. This paper reviews shock waves in highly enriched material in supernova remnants (SNRs) and the nebular phase of some supernovae. It does not deal with the shocks in the interior of the exploding supernova where nuclear processing occurs.

✉ J.C. Raymond
jraymond@cfa.harvard.edu

[1] Center for Astrophysics, 60 Garden St., Cambridge, MA 02138, USA

The first difference between normal shocks and ejecta shocks is the larger mean particle mass, μ. For fully ionized gas of astrophysical abundances, $\mu = (n_H + 4n_{He})/(2n_H + 3n_{He})$ times the proton mass, where the denominator is the number of electrons plus the number of nuclei, or 0.6. For a fully ionized oxygen plasma, however, μ is $16/9 = 1.78$, and for fully ionized iron it is $56/27 = 2.07$. The difference becomes much more severe if the gas is partially ionized, for instance at a temperature of 10^5 K. In that case there are far fewer electrons per atom, perhaps 2 for the oxygen plasma and 4 for Fe, so that μ is 5.3 or 11.2, respectively.

The value of μ enters the shock jump conditions directly. For a strong shock,

$$T = \frac{3}{16} \frac{\mu m_p}{k} V_s^2 \tag{1}$$

for a ratio of specific heats $\gamma = 5/3$, where k is the Boltzmann constant, or

$$T = 1.36 \times 10^5 \mu_{0.6} V_{100}^2 \tag{2}$$

where V_{100} is the shock speed in units of 100 km/s. Thus for normal abundances, a 100 km/s shock heats the gas to 1.36×10^5 K. For fully ionized oxygen it would be 3.8×10^5 K, but if the oxygen is only doubly ionized it would be 1.1×10^6 K. A 100 km/s shock in pure iron would produce $T = 4.5 \times 10^5$ K if the plasma is fully ionized, or 2.4×10^6 K if it is 4 times ionized. These estimates assume equal electron and ion temperatures, but as discussed below that is unlikely to be the case. Moreover, the ionization state will change rapidly once the gas is heated, and the immediate post-shock temperature will have little relation to the ionization state seen by an observer.

The second difference between shocks in gas of normal abundances and those in ejecta is the far larger cooling rate in the latter. At temperatures above about 30,000 K, hydrogen is fully ionized, and it emits radiation mainly by the inefficient processes of Bremsstrahlung and radiative recombination. The heavy elements that retain bound electrons, on the other hand, produce strong emission lines, and the radiative cooling rate in the shocked ejecta is 1 to 3 orders of magnitude larger than in normal abundance gas at the same temperature.

Figure 1 shows the cooling rate coefficients Λ as functions of electron temperature for normal astrophysical abundances and for pure oxygen, silicon and iron. The power emitted is

$$P = \Lambda(T_e) n_i n_e \text{ erg}/(\text{cm}^3 \text{ s}) \tag{3}$$

computed with CHIANTI version 8 (Del Zanna et al. 2015). n_i is the density of H nuclei for the normal abundance case, and the density of O, Si or Fe nuclei in the others. Note, however, that these curves assume that the plasma is in ionization equilibrium, and as discussed below this is often a poor approximation in shocked ejecta gas.

The character of the emission is apparent from Fig. 1. At the highest temperatures, all the ions are stripped bare, and the emission is dominated by the bremsstrahlung continuum, which is approximately proportional to Z^2 and increases as $T^{1/2}$. Thus Λ is roughly proportional to Z^2. At lower temperatures where emission lines dominate, the ratio of Λ to the solar abundance cooling rate is closer to ratio of the abundance to the solar value, or around 2000 where oxygen dominates at Log $T \sim 5.2$ to5.5, even at normal astrophysical abundances. The line-to-continuum ratio, or equivalent width (EW) is the basis for determining elemental abundances from X-ray spectra. When the continuum is dominated by bremsstrahlung, it is proportional to the abundance divided by Z^2.
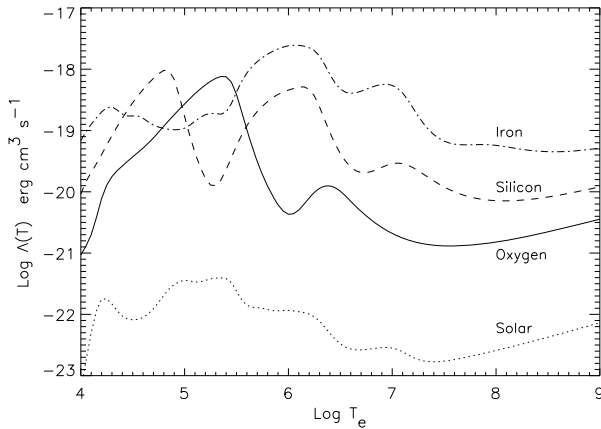
Fig. 1 Cooling rate coefficients for solar abundances (Grevesse et al. 2007) and for pure O, Si and Fe as functions of electron temperature. These rates assume collisional ionization equilibrium, which is generally a poor assumption for shocks, but they give a general idea of the relative magnitudes and rough temperature dependence. The smoothly rising rates at the highest temperatures are dominated by bremsstrahlung emission with a contribution from radiative recombination, while the cooling at lower temperatures is dominated by line emission. The bumps and dips in the curves correspond to the shell structure of the dominant ions. The drop in Λ_O between 2×10^5 K and 10^6 K occurs because oxygen is ionized to the stable He-like and H-like states that have no electrons that are easy to excite. The dip in Λ_{Si} at about 1.5×10^5 K is where Si is Ne-like, and the drop above 2×10^6 K is where it becomes He-like. The Λ_{Fe} curve dips where Fe is Ne-like at 3×10^6 K and above 1.5×10^7 K where it becomes He-like. These cooling rates were computed with CHIANTI (Del Zanna et al. 2015)

The consequence of the large cooling rate is a very short cooling time scale. Under normal conditions, the radiative cooling time is generally comparable to or longer than the Coulomb collisional time scales for energy transfer between electrons and ions and among different ion species, but in ejecta shocks that is not true (Itoh 1981a). Radiative cooling time scales are typically longer than ionization and recombination times at temperatures above 10^6 K in normal abundance plasma, while they are much shorter in the ejecta, meaning that time-dependent ionization (non-equilibrium ionization or NEI) is much more important. While the rapid cooling might be expected to make radiative cooling dominate over energy transfer processes such as thermal conduction, the rapid cooling makes the cooling length very short, and the strong temperature gradient makes the divergence of thermal conduction quite important in the absence of a magnetic field (Borkowski and Shull 1990).

Another implication of the rapid cooling is a change in the character of fluid instabilities. The cooling zone behind a shock is subject to thermal instability over a wide range of shock speeds in normal gas (Chevalier and Imamura 1982; Innes et al. 1992; Gaetz et al. 1988) This instability leads to violent collapse, secondary shocks and large swings in the shock speed itself, though magnetic fields can cushion the effect (Innes 1992). A higher cooling rate will enhance this instability. Another instability, called the thin shell instability (Vishniac 1983), occurs when a thin, dense shell created by a radiatively cooling shock is driven by hot, high pressure gas behind it. Ripples in the shell grow because the ram pressure of gas entering the shell lies along a different direction than the pressure force from the inside. A high cooling rate means that a shell prone to the Vishniac instability is established very quickly.

This paper discusses the above points as they relate to observations of the reverse shocks in SNRs and supernovae, paying particular attention to their implications for the accuracy

with which one can infer elemental abundances and other physical parameters from spectra. Sections 2 and 3 distinguish between collisional vs. collisionless shocks and radiative vs. non-radiative shocks. Sections 4 and 5 discuss electron-ion and ion-ion temperature equilibration. Sections 6, 7 and 8 discuss the roles of the photoionization precursor, fluid instabilities and cosmic ray acceleration in the reverse shock, and Sect. 9 covers the reliability of shock parameters inferred from spectra and models. Those sections address shocks in supernova remnants, while shocks in the ejecta of supernova themselves (taken here to be less than about 100 years old) are discussed in Sect. 10. Section 11 is a summary discussion of the reliability of abundances and other parameters inferred from spectra of shocks in highly enriched ejecta. A brief Appendix lists O-rich SNRs and some recent observations. The important question of dust destruction by sputtering and grain-grain collisions is covered in separate papers in this volume (Micelotta et al. 2017; Sarangi et al. 2017).

2 Collisional and Collisionless Shocks

A shock wave converts a supersonic flow to a subsonic one both by decreasing the flow speed in the rest frame of the shock and by increasing the sound speed by increasing the temperature. The decrease in flow speed must be accompanied by compression in order to conserve mass flux. The increase in sound speed results from the conversion of kinetic energy of the bulk flow into thermal energy. The transition from pre-shock to post-shock conditions is sharp, because the supersonic speed does not allow information about the approaching shock to be carried upstream by sound waves.

In a collisional shock, such as a weak shock in air, the transition is mediated by collisions between particles, so the thickness is approximately a collisional mean free path. Collisions lead naturally to a Maxwellian distribution in order to maximize entropy, and for the same reason they lead to thermal equilibrium among different particle species; all the species reach the same temperature.

In a plasma, the transition can occur on a scale much shorter than the collision scale. One natural scale is the proton Larmor radius, R_L. For typical ISM conditions, the collision scale is on the order of 10^{15} cm, while R_L is on the order of 10^8 cm. Another scale is the proton skin depth, given by the speed of light divided by the proton plasma frequency. It characterizes electrostatic waves that interact with the protons, and $L_s = c/\omega_p = 1.4 \times 10^8/n^{1/2}$ cm, which is comparable to the Larmor radius for typical conditions in the interstellar medium (ISM).

In collisionless shocks, a particle interacts not with another particle, but with the collective effects of a large group of particles. There is no obvious reason to expect Maxwellian distributions or equal temperatures of different species, and in fact particle acceleration and differences among proton, electron and heavier ion temperatures are often observed in shocks in the solar wind and in the ISM. A large range of complex plasma processes comes into play. Some protons are reflected from the shock, and the resulting two-stream instabilities generate plasma waves. The more energetic particles can scatter between the shock and magnetic turbulence in a shock precursor, gaining energy each time and reaching relativistic speeds. Magnetic fields can be amplified beyond the values given by compression of the upstream field.

Shocks in plasmas are divided into quasi-perpendicular and quasi-parallel based on the angle between the shock normal and the local magnetic field. The former tend to be more laminar, while the latter are more turbulent. The quasi-parallel shocks are generally thought

Fig. 2 Temperature structure of the post-shock flow in a radiative shock. This steady flow model from an updated version of the Raymond (1979) model does not include thermal conduction or the thermal instability that affects shocks above about 150 km/s
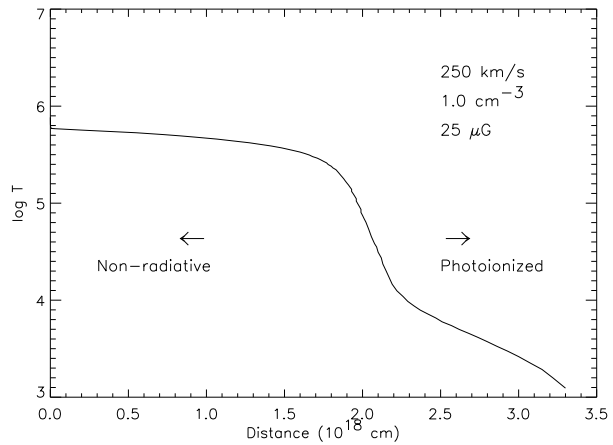
to be able to accelerate more particles, while the quasi-perpendicular ones accelerate particles more quickly, though turbulence, magnetic field irregularities and ripples in the shock can blur the distinction (Giacalone 2013).

Observations of the consequences of collisionless shock physics in ejecta shocks are sparse. In subsequent sections we describe what is known about shocks in normal abundance plasmas from observation and simulation, then what is known about the shocks in ejecta.

3 Radiative and Non-Radiative Shocks

It is convenient to divide shocks into radiative and non-radiative classes based on the global situation rather than the physics in the shock itself. A non-radiative shock is one in which the radiative cooling time of the shocked gas is long compared to other dynamical time scales. For instance, the blast wave in a young SNR produces temperatures of order 10^8 K, and the radiative cooling time is much longer than the age of the SNR. Therefore, radiative cooling does not have time to convert much of the post-shock thermal energy into radiation or to affect the dynamics of the flow. The X-ray emission in SNRs is mostly produced by non-radiative shocks. The gas that has gone through a radiative shock, on the other hand, has time to cool to something like the pre-shock temperature.

The radiative cooling time for normal abundance gas (at constant pressure) is given by

$$t_{cool} = \frac{5}{2}(n_e + n_i)kT/(n_e n_i \Lambda) \sim 5\, kT/(n_e \Lambda), \tag{4}$$

where $n_e \simeq n_i$ in a plasma dominated by hydrogen. Over much of the interesting temperature range above $T \sim 3 \times 10^5$ K, Λ decreases with increasing T, so that t_{cool} increases rapidly with V_S. As a result, there is a strong tendency for SNR shocks in the ISM faster than about 300 km s^{-1} to be non-radiative and slower shocks to be radiative. Because of the fact that by definition radiative shocks convert much of their thermal energy to photons, radiative shocks tend to be much brighter and easier to observe in the optical, infrared (IR) and ultraviolet (UV).

From the point of view of plasma kinetics, emission that is produced in the neighborhood of a non-radiative collisionless shock will reflect such things as departures from Maxwellian distributions or temperature differences among particle species. Radiative shocks, on the

other hand, produce radiation by collisions at somewhat comparable rates to the Coulomb collisions that bring the gas toward thermal equilibrium. Thus most of the signatures of plasma processes in the shock will have been erased by the time the gas produces the bright emission that dominates the spectrum.

Figure 2 illustrates the structure of a radiative shock in the normal ISM, in this case a 250 km/s shock with a pre-shock density of 1 cm^{-3}. If the shock has progressed a short distance into the medium so that a post-shock layer thinner than about 10^{18} cm has accumulated, it is effectively non-radiative in that cooling has not greatly changed the temperature or dynamics of the flow. Beyond that, cooling abruptly drops the temperature to about 10^4 K. Still farther behind the shock, photoionization maintains an H II region-like zone, often supported by the pressure of the compressed magnetic field, where the temperature gradually declines as the ionizing flux is absorbed away. Note that this is an idealized steady-flow model. Shocks in this velocity range are subject to drastic thermal instability after they become radiative (e.g. Innes 1992), as discussed below.

Ejecta shocks can be divided in the same way into radiative and non-radiative classes, but of course t_{cool} is orders of magnitude shorter for a given density and temperature. This is offset to a limited extent by the higher temperature produced by a given shock speed. In general the shock in the ejecta is the reverse shock in an SNR or type IIn SN, produced when the unshocked ejecta encounters the high pressure shell formed by the blast wave. To the extent that the pressure in that region is uniform, the ram pressures ρV_S^2 of different parts of the reverse shock are the same. The ejecta in Cas A and other O-rich SNRs consist of dense clumps embedded in a lower density gas. The reverse shock in the low density gas is non-radiative, and it produces the strong X-ray emission. The slower reverse shocks in the small, dense clumps are radiative, and they as seen as the optical knots. The optical knots make up a small fraction of the volume and mass. In type I SNRs like Tycho and SN1006, the ejecta are more uniform, and the ejecta shocks are entirely non-radiative, though diffuse clumps are seen, probably as a result of the Rayleigh-Taylor instability of the contact discontinuity between the shocked ejecta and shocked ISM (e.g., Blondin and Ellison 2001).

Because of the enormous cooling rate, even radiative shocks in the ejecta can maintain signatures of the plasma processes in the shock. Most importantly, the cooling time can be shorter than the Coulomb equilibration time even at modest temperatures, so electron and ion temperatures can be drastically different.

4 Electron-ion Thermal Equilibration

As mentioned above, there is no a priori reason to expect thermal equilibrium among different particle species behind a collisionless shock, and there is strong observational evidence for large differences between electron and ion temperatures in shock waves in the solar wind and in fast shocks in the ISM. In principle, one might expect that since the protons carry 1840 times as much kinetic energy as the electrons when they enter the shock, they would be up to 1840 times hotter when the kinetic energy is transformed into thermal energy. Itoh (1978) computed models of SNR blastwaves in which the electrons and ions were treated as separate fluids coupled by Coulomb collisions. In those models the electrons were cool at the shock, and the Coulomb collisions heated them fairly rapidly to $kT = 1$–2 keV in young SNRs, at shock speeds that gave ion temperatures 10 times higher or more.

Several theories have been advanced that provide varying degrees of collisionless electron heating at the shock. Cargill and Papadopoulos (1988) proposed a sequence of instabilities driven by ions reflected from a fast shock (Mach number $M > 20$). The Buneman

instability heats the electrons quickly, but it saturates at a fairly low electron temperature. It can, however, permit the ion acoustic instability to heat the electrons to perhaps 30% of the ion temperature. Bykov and Uvarov (1999) examined electron heating by diffusion in the turbulent magnetic precursor of a quasi-parallel shock predicted by a hybrid code. Shimada and Hoshino (2000) performed particle-in-cell (PIC) simulations and found that electrostatic waves driven by streaming instabilities could heat the electrons to about 20% of the ion temperature. Ghavamian et al. (2007a) and Rakowski et al. (2008) showed that streaming cosmic rays in the shock precursor can drive lower hybrid waves that can effectively couple electrons to ions. Their model predicts $T_e/T_i \propto 1/V_S^2$ for shocks faster than about 300 km/s, though Laming et al. (2014) find that there can be additional electron heating in very fast shocks.

Other theories rely on the electric field on the shock. In general, the electrons must interact with electromagnetic fluctuations or turbulence of some sort in order to be confined in the region where the electric field exists if they to be significantly heated (Hull et al. 2000; Ohira and Takahara 2007; Mozer and Sundkvist 2013; Schwartz 2014). The electron heating is closely tied to the injection of electrons into the non-thermal acceleration mechanism. Numerical simulations by Riquelme and Spitkovsky (2011) show an electron distribution with a Maxwellian core and a power law tail. In their simulations there is a high degree of electron-ion equilibration close to the shock for some shock parameters.

Detailed reviews of electron-ion thermal equilibration are given by Ghavamian et al. (2013) for shocks in normal astrophysical gas and Bykov et al. (2008) for galaxy clusters. A thermodynamic approach to thermal equilibration in shocks is given by Vink et al. (2015). Here we summarize the major points and consider the case of shocks in SN ejecta.

4.1 Non-Radiative Shocks

Electron-ion temperature ratios can be measured in several ways. Instruments on spacecraft in the solar wind measure electron and ion temperatures directly from the velocity distribution functions. Bow shocks form around the magnetospheres of the Earth and other planets, and both coronal mass ejections (CMEs) and interactions between solar wind flows of different speeds drive shock waves in the solar wind. At Earth, the solar wind temperature is on the order of 10^5 K, and the shocks range from very weak to those of Mach numbers (shock speed divided by sound speed) of order 10. Schwartz et al. (1988) measured the heating of electrons and ions that passed through these shock waves and found on average $T_e/T_p \sim 0.2$ with considerable scatter. The scatter could be due to differences in the shock normal angle, since quasi-parallel and quasi-perpendicular shocks are expected to behave very differently.

T_e/T_p has also been determined by remote sensing observations of a few CME-driven shocks in the solar corona. Bemporad et al. (2014) combined UV spectra and White Light coronagraph images and found a range of about 0.16 to 0.8 for shocks with Mach numbers below or about 2. On the other hand, Ma et al. (2011) determined the electron heating in another low Mach number CME-driven shock in the corona based on narrow band EUV images from the AIA instrument aboard SDO. They found an electron temperature consistent with the shock speed and full electron-ion temperature equilibration. In this case the electron heating is determined from the evolution of the ionization state in the downstream gas.

Another way to measure electron and ion temperatures uses the Hα profiles of collisionless shocks in partly neutral gas. The profiles consist of a narrow component produced by atoms that pass through the shock unaffected by the fields and turbulence in the narrow shock layer, and a broad component produced by atoms that experience charge transfer

collisions with post-shock protons (Chevalier and Raymond 1978). The broad component gives the proton temperature fairly directly, since its width is given by the proton temperature convolved with the charge transfer cross section times the speed. The intensity ratio of broad and narrow components is sensitive to the electron temperature because it depends on the ratio of ionization rate (by electrons) to charge transfer rate. The velocity width of the narrow component is generally higher than would be consistent with the ambient ISM temperature for neutral gas, indicating the presence of a shock precursor (Hester et al. 1994; Smith et al. 1994; Sollerman et al. 2003; Ohira 2014; Lee et al. 2007, 2010).

An advantage of this method is that it applies to the region close to the shock where H has not yet been ionized, and that means that there has not been time for Coulomb collisions to affect T_e/T_i. In terms of column density, the Hα emission from the Balmer line shocks comes from a region within about 10^{15} cm^{-2} from the shock. The possible contribution of the precursor to the narrow line intensity is the main limitation to the accuracy of the T_e determination, but radiative transfer of the Lyβ photons (Chevalier et al. 1980) also enters. This diagnostic has been applied to supernova remnant shocks between about 350 and 2500 km/s, and T_e/T_p is near one in the slower shocks and less than 0.1 in the fast ones (e.g. Ghavamian et al. 2001; Medina et al. 2014; Ghavamian et al. 2013).

A third means of measuring electron heating is by measuring the shape of the X-ray continuum, since bremsstrahlung produces an $e^{-h\nu/kT_e}$ spectral shape. The proton temperature can be obtained from the Hα profile method described above or from the shock speed obtained from proper motions. Again, shocks near 300 km/s show $T_e/T_p \sim 1$ (Salvesen et al. 2009), while shocks above 1000 km/s show $T_e/T_p \sim 0.1$ or less (Rakowski et al. 2003; Long et al. 2003; Kosenko et al. 2008; Helder et al. 2011; Hovey et al. 2015). Hughes et al. (2000) estimated a shock speed of 6000 km/s from the expansion proper motion of 1E102.2-7219 in the SMC, and that resulted in $T_e/T_p < 0.04$, but a recent measurement of the expansion rate from Chandra images indicates a slower shock and an electron-ion temperature ratio several times higher (Plucinsky and Gaetz, private communication). Thus these results agree with those from Balmer line profiles, and they can be applied to shocks in fully ionized plasma as well as partly neutral gas. A limitation of this method is the finite resolution of the X-ray telescope, generally implying a region at least 10 to 100 times thicker than the region where Hα emission is produced. Therefore, it is subject to the effects of Coulomb collisions.

Figure 3 shows some results from the above methods for shocks in the solar wind and the normal ISM (Ghavamian et al. 2013). The X-axes in the three panels show how T_e/T_i scales with shock speed and Mach number (V_S divided by characteristic signal speed) for the Alfven speed or fast mode speed. All three of the scalings show some disconnect between the solar wind shocks and the generally faster ISM shocks, but the general trend for fast shocks to be less equilibrated than slow ones is seen in both sets of data. A few points show T_e/T_i ratios above 1, which is not generally predicted by shock models, but those points may result from non-local effects such as thermal conduction or non-Maxwellian electron velocity distributions which occur in the solar wind.

Yet another way to infer T_e/T_p is presented by Laming et al. (1996), who used the UV spectrum of SN1006 obtained by the Hopkins Ultraviolet Telescope to measure the intensities of lines of He II, C IV, N V and O VI. Because of its high excitation potential, the He II λ1640 Å line is dominated by electron collisions, while the other lines are excited mainly by collisions with protons and α particles. In agreement with the results of other studies of the northwestern (NW) region of SN1006 based on Hα profiles and X-ray spectra, Laming et al. (1996) found $T_e/T_p \leq 0.2$.

It is more difficult to measure T_e/T_i in shocks in SN ejecta. The electron temperature can be measured from the X-ray continuum shape, but it is difficult to determine the ion
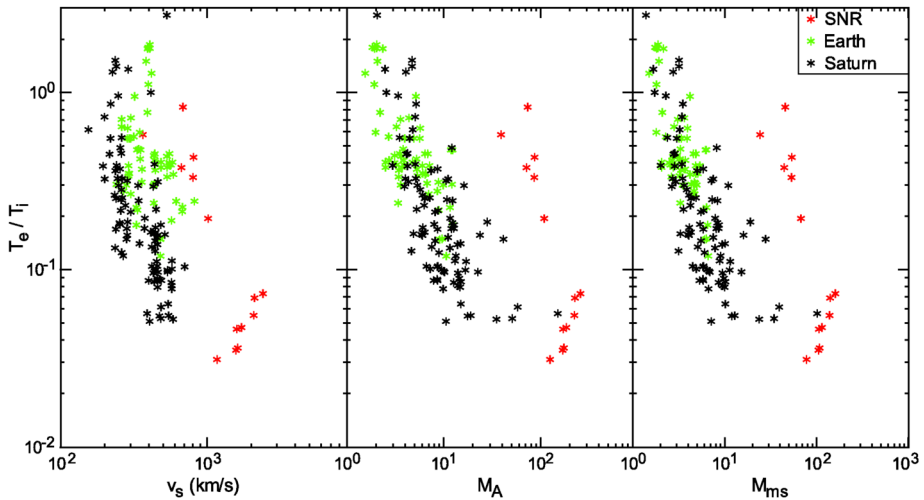
Fig. 3 Comparison of electron-to-ion temperature ratios for solar wind shocks (*black* and *green*) and supernova remnant (*red*) shocks. The X-axes show how the values depend on shock speed, Alfven Mach number and fast mode (magnetosonic) Mach number. From Ghavamian et al. (2013)

temperature. Measurements of the O VII emission line profile in an ejecta knot in SN1006 give a value of the kinetic temperature T_O of 275 keV, compared with an electron temperature of 1.35 keV (Vink et al. 2003; Broersen and Vink 2014), so that T_e/T_O is about 0.005 in this 3000 km/s shock. Another method was introduced by Yamaguchi et al. (2014), who measured the Fe Kα and Kβ centroids and the intensity ratio of the two lines. These depend on the ionization state of the Fe because of different energies and fluorescence yields of ions less ionized than He-like, as shown in Fig. 4. This allowed Yamaguchi et al. (2014) to determine the electron temperature in the reverse shock in Tycho's SNR. They find that T_e/T_{Fe} is about 0.01 in the ∼4000 km s^{-1} reverse shock. Kosenko et al. (2008) observed the type Ia SNR 0509-76.5 in the LMC with XMM-Newton. They used a global model for the continuum and Fe emission and found T_e/T_i in the range 0.003 to 0.03, but this includes both the blast wave and the reverse shock.

A very direct upper limit to the electron heating in a reverse shock of SN1006 is given by Hamilton et al. (2007). They measured the absorption in the Si II λ1260 line from both the shocked and unshocked ejecta of SN1006 against a background star. A fit to the line profile yields the pre- and post-shock speeds and the post-shock temperature. The 2700 km/s shock speed derived from the difference between pre-and post-shock speeds and the post-shock temperature are consistent with the shock jump conditions with no electron heating, and Hamilton et al. (2007) find a 3σ upper limit on the fraction of energy that goes into electrons of 0.26.

Figure 5 shows models in which plasma turbulence heats the electrons to 1% of the ion temperature, and then Coulomb collisions gradually bring the electron and ion temperatures together. It is sensible that only Coulomb collisions should act in the region away from the shock transition because the turbulence associated with the shock should die out rapidly, but this assumption has not been tested. The shock speeds were chosen to give similar T_e and T_i downstream, and the pre-shock ion densities are the same. An unsubtle difference between the normal abundance shock on the left and the pure oxygen shock on the right is the order of magnitude difference in the scales of the X-axes. This is mostly due to the Z^2 factor in
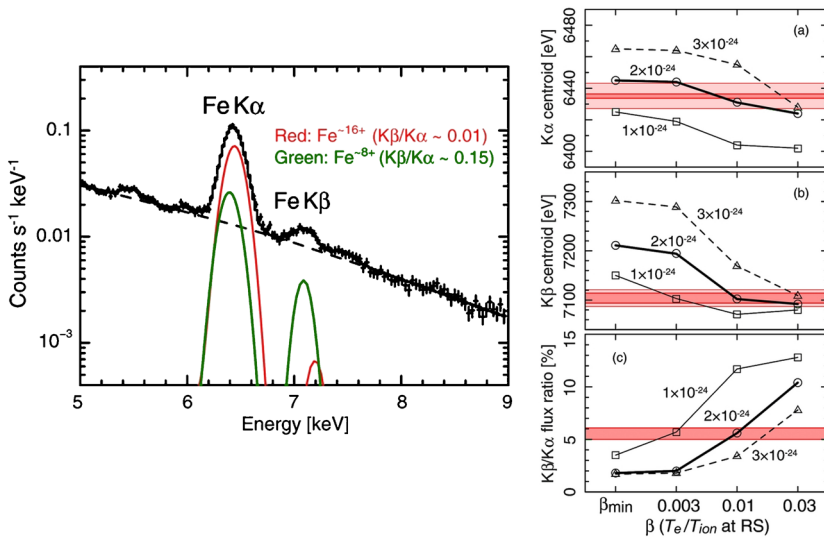
Fig. 4 Dependence of the centroids and the intensity ratio of the Fe Kα and Kβ lines on the ionization state of Fe in the reverse shock of Tycho's SNR (Yamaguchi et al. 2014). The *lines in the right hand plots* correspond to ambient densities of 1, 2 and 3×10^{-24} g/cm^3

Fig. 5 Non-radiative shocks in normal abundance plasma (*left*) and pure oxygen (*right*). Note the different scales on the X-axes. The models assume that $T_e = 0.01 T_i$ at the shock and that Coulomb collisions subsequently bring the plasma toward equilibrium
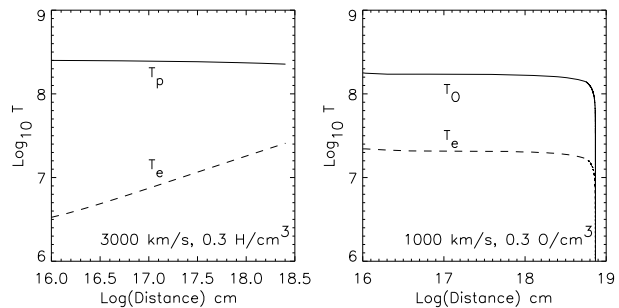
the Coulomb collision rate. A more subtle difference is the drop in T_O shortly behind the pure oxygen shock. It occurs as the O ions share their energy with 8 electrons per ion and as radiative cooling by the L-shell oxygen ions O II–VI converts some of the thermal energy into photons. In the constant T_e region in the ejecta shock model, radiative cooling of the electrons nearly balances the transfer of heat from ions to electrons by Coulomb collisions.

Itoh (1977) constructed hydrodynamic models of the non-radiative shocks in Cas A assuming either $T_e = T_i$ or no electron-ion equilibration other than by Coulomb collisions. The latter gave good agreement with the X-ray spectra available at the time, while the complete equilibration model predicted far too much emission at high energies. It is now known that a substantial fraction of the higher energy X-ray spectrum arises from synchrotron emission from non-thermal electrons (Helder and Vink 2008), so the constraints on T_e are even more severe.
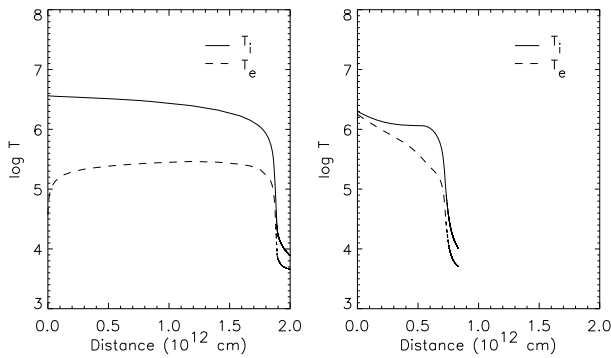
Fig. 6 Radiative 100 km/s shocks in oxygen at a density of 100 cm^{-3}. The *left panel* shows a case with $T_e = 0.01T_O$ at the shock, and *the right* shows $T_e = 0.90T_O$. In the *left panel*, the initial low T_e gives very rapid Coulomb heating of the electrons until they reach about 2×10^5 K. There is a long plateau in which heating by Coulomb collisions nearly balances the radiative losses, but it ends when the oxygen ions run out of energy, and the temperature collapses. In the *right panel*, the electron and ion temperatures start out nearly equal, but the rapid radiative cooling causes T_e to drop to a fraction of T_O. The initial drop in T_O results from the increase in the number of electrons sharing the energy, and the subsequent plateau in T_O is analogous to that in the *left panel*. The cooling length is shorter because of faster cooling at the higher electron temperatures. Again, it collapses, and both temperatures drop rapidly

4.2 Radiative Shocks

Itoh (1981a,b) performed the first calculations of a radiative shock in pure oxygen and compared them with observations of Cas A. He found that whether or not the electron and ion temperatures were equilibrated at the shock, the intense cooling of the electrons caused T_e to be well below T_O through most of the flow. Figure 6 shows the electron and ion temperatures for 100 km/s shocks in pure oxygen. The temperature structures and even the cooling lengths depend upon the degree of electron-ion thermal equilibration at the shock front, but in either case the electrons are much cooler than the ions in most of the flow. Itoh (1986) found some difficulties in matching the spectra of observed O-rich SNRs. In particular, the flow had to be artificially truncated in order to avoid overpredicting the permitted O I recombination lines at $\lambda\lambda7774$, 8446 Å, and the models had difficulty predicting strong enough emission in the [O I] $\lambda\lambda6303$, 6363 Å forbidden lines. This led Itoh (1988) to suggest that simple planar models were not adequate, and that unsteady flows or turbulent stripping in the shearing flows at the edge of the knots were important.

Laboratory experiments and their supporting numerical simulations provide confirmation of the large differences between ion and electron temperatures when shocks travel through material with large cooling rates. Measurements of laser-produced shocks in xenon by Grun et al. (1991) were successfully modeled by Laming and Grun (2002) with simulations in which only Coulomb collisions heat the electrons and T_e/T_{Xe} ranges from about 0.01 to 0.1 in the post-shock flow. Suzuki-Vidal et al. (2015) studied bow shocks driven by electrical current pulses in aluminum foils, and their models showed T_e/T_{Al} around 0.1 in the post-shock flow. Both of these experiments focused on the fluid instabilities that result from the intense cooling, and those instabilities are discussed below.
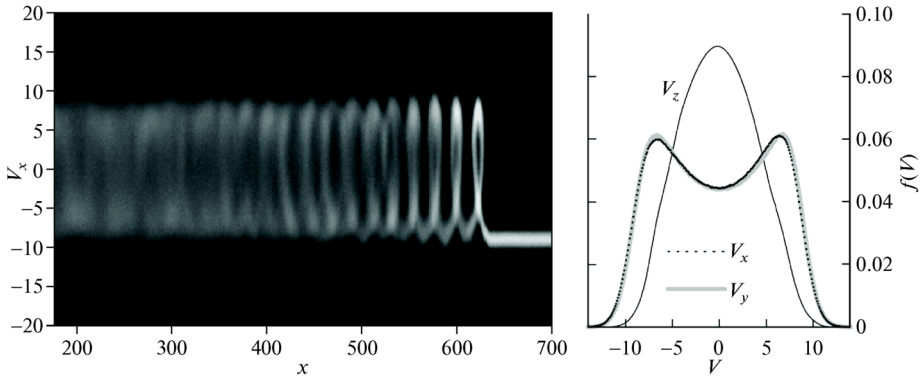
Fig. 7 Phase space and integrated velocity distributions for Fe II impurity ions in Si III background gas from a hybrid simulation by Kropotina et al. (2015). In the *left panel*, x is in units of the Si III inertial length. The V normalization is the inertial length times the cyclotron frequency, i.e., the Alfvén speed. This figure shows a quasi-perpendicular shock with Alfvén Mach number $M_A = 9$ and plasma beta parameter $\beta = 1.0$

5 Ion-Ion Thermal Equilibration

Ion-ion thermal equilibration could be different from electron-ion equilibration. For instance, the charge-to-mass ratio Z/A is typically 2 to 5 times smaller for heavy ions than for protons, and this is a very small difference compared to the value of 1840 for electrons vs. protons. Thus energy transfer that depends on plasma waves that interact resonantly with both species is much more difficult for electrons than for ions (Kropotina et al. 2015, 2016). Measurements of ion heating in shocks in the solar wind generally show $T_i > T_p$ (Berdichevsky et al. 1977; Korreck et al. 2007), and some models predict strong preferential heating, with $T_i > (m_i/m_p)T_p$ and asymmetry such that $T_\perp > T_\parallel$ (Zimbardo 2011).

Thus ion temperatures present interesting diagnostic capabilities, and the degree of equilibration between He and H ions influences the interpretation of Hα line widths in Balmer-dominated shocks in terms of shock speed (Chevalier et al. 1980). Figure 7 shows the distribution of Fe II impurity ions behind a quasi-perpendicular shock (Kropotina et al. 2015).

The Hopkins Ultraviolet Telescope (Kruk et al. 1995) was used to observe lines of He II, C IV, N V and O VI in a 2300 km/s shock in the NW part of SN1006 blast wave (Raymond et al. 1995). Line widths were measured for the He II λ1640 and C IV λ1550 lines and compared with the Hα line width from Smith (1991). The result was that the thermal speeds were all the same to within measurement uncertainties of 10 to 24%, indicating that the temperatures are mass-proportional; $T_a = (m_a/m_p)T_p$. Subsequently Korreck et al. (2004) used FUSE to observe the same position in O VI and obtain a kinetic temperature that was mass-proportional to the He and C temperatures within the uncertainties, but formally only half the 2.9×10^9 K value that would be mass-proportional to the proton temperature. That paper assumed a 3000 km/s shock speed based on Ghavamian et al. (2002), and the formal uncertainty of the O VI line width may be optimistic due to severe blending with Lyβ.

While the very fast blast wave in SN1006 showed little or no ion-ion thermal equilibration, the 350 km/s blast wave in the Cygnus Loop shows very strong equilibration, with T_{He}, T_C and T_O equal to T_p to within the uncertainties (Raymond et al. 2015). This is in accord with the effective electron-ion equilibration in this section of the Cygnus Loop (Ghavamian et al. 2002; Salvesen et al. 2009; Medina et al. 2014). Estimates of T_O/T_p in DEML71, which has intermediate shock speeds of about 650 and 900 km/s, are 6.5 and 16, suggesting partial equilibration at 650 km/s and no equilibration at 900 km/s (Ghavamian et al. 2007b).

Broersen et al. (2013) measured the width of the O VII X-ray lines in an ejecta knot in SN1006 using the RGS on XMM-Newton. As mentioned above, it indicated very little electron-ion temperature equilibration. The line width corresponds to a shock speed of 3000 km/s if there is no equilibration. They could not measure the widths of other lines, but a low resolution X-ray spectrum showed strong Si emission, implying that the Si abundance was enhanced 6 or 7 times more that the O abundance. That would mean that if there is significant ion-ion equilibration, O would be heated by the Si and a slower shock would give the observed line width. Unfortunately, while the speed of the shock driven into the ISM by the ejecta knot can be determined from its Hα profile or its proper motion, we do not know the speed of the reverse shock that heats the ejecta.

An interesting possible modification of ion-ion equilibration can occur if some of the elements passing through the shock are neutral while others are completely ionized. For instance, some of the hydrogen going into Balmer line shocks is neutral, while elements whose ionization potentials are less than the energy of Lyα photons (10.2 eV) or of the Lyman edge at 13.6 eV are likely to be singly ionized in the pre-shock gas. The ions interact with the fields and turbulence at the shock, while the neutrals are not affected. When they become ionized well downstream, the turbulence is likely to have decayed away, and the newly formed ions behave as pickup ions (Williams and Zank 1994). When they are ionized, the velocity components parallel and perpendicular to the field are conserved, and the perpendicular component quickly evolves into a shell in velocity space. In the process the ions generate plasma waves at their Larmor frequency, but those waves do not interact strongly with other ion species. This pickup ion behavior has been suggested as a possible explanation for the non-Gaussian line profile seen at one position in Tycho's SNR (Raymond et al. 2008, 2010), but that is only one of four plausible explanations. Something similar could occur in an ejecta shock propagating through a mixture of O (I.P. = 13.6 eV), Ne (I.P. = 21.6 eV), Si (I.P. = 8.2 eV) and Fe (I.P = 7.9 eV), but as yet there are no observations of ejecta shocks that could test this idea. However, even the higher IP neutrals may be photoionized before they reach the reverse shock, as discussed in the next section.

6 Photoionized Shocks and Precursors

Photoionization enters the picture in three ways. First, radiative shocks by definition effectively convert the thermal energy of the shocked gas into radiation, and if the electron temperature is above about 10^5 K, much of that is ionizing radiation. That radiation is always included in computing the spectrum emitted by the cooling gas, and it can also produce a photoionized precursor whose strength depends on the evolution of the shock as it passes through the cloud. Second, non-radiative shocks produce some emission, both in the X-rays and in UV lines from lower ionization as the shocked gas becomes ionized (Hamilton and Fesen 1988). That radiation can be important in the unshocked ejecta. And, third, a pulsar wind nebula (PWN) can ionize the shocked gas. Though all three can occur simultaneously, we consider them separately for simplicity.

6.1 Photoionized Precursors to Radiative Shocks

Photoionization precursors can be seen ahead of radiative shocks in normal abundance gas. Figure 8 shows a deep Hα image of a portion of the Cygnus Loop, and the faint, diffuse emission at about 20^h 57^m 30^s is the pre-shock cloud photoionized by the EUV radiation from the bright radiative shocks at lower RA. In this case, the precursor is easily spatially
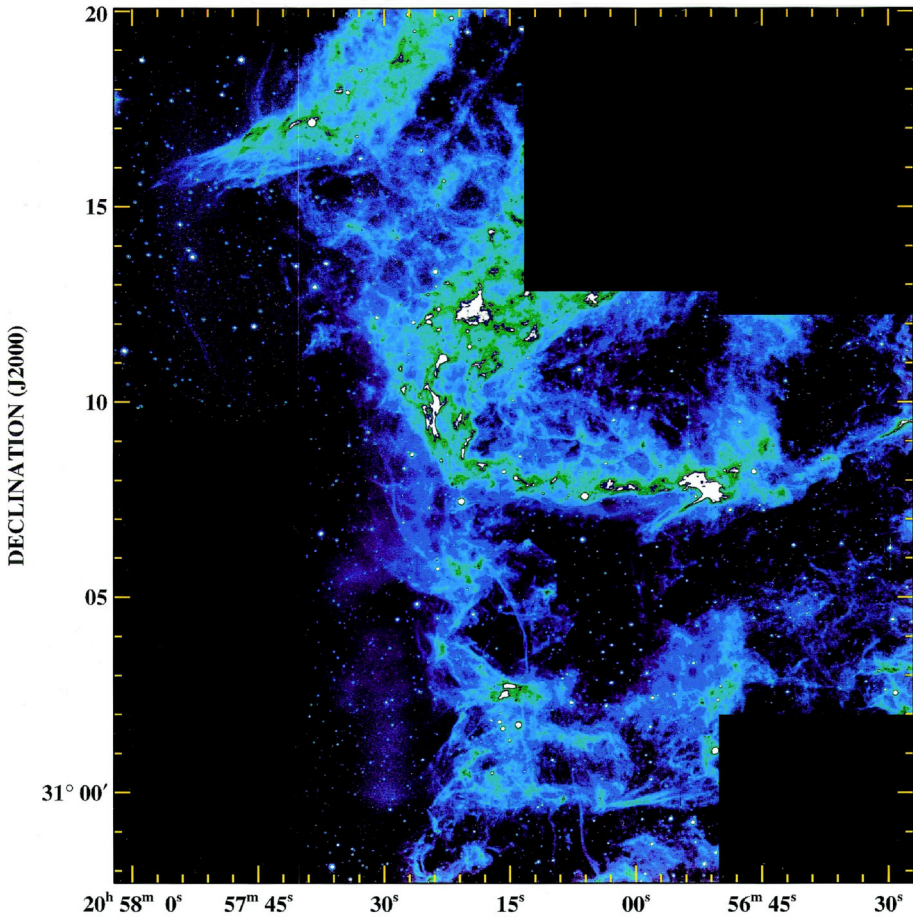
Fig. 8 Hα image of a portion of the Cygnus Loop showing vertical stripe of faint diffuse emission ahead of the shock (at higher RA) near $20^h\ 57^m\ 30^s$ between about $+31°0'$ and $+31°3'$ in declination (Szentgyorgyi et al. 2000). At the distance to the Cygnus Loop, $5'$ corresponds to roughly 1 pc

resolved from the shocked gas, but in more distant SNRs in denser gas that may not be the case.

The early models of shocks in pure oxygen by Itoh (1981a) were not able to match all the line ratios. Itoh (1981b) included a photoionization precursor in his models, but they still had difficulties with some line ratios. Subsequent calculations by Dopita et al. (1984) included other elements besides oxygen. They also found that the models failed to match observed spectra. In particular, the temperature-sensitive ratios [O III] I(4363)/I(5007) and [O II] I(7320,30)/I(3726, 29) were predicted to be much too high in the models. Blair et al. (1989) and Blair et al. (1994) obtained UV spectra of 1E102-7219 and N132D with IUE, and they found basically the same difficulty that Dopita et al. (1984) pointed out. If T_e is high enough to produce the observed ions by collisional ionization, then the models predict UV to optical line ratios larger than observed. This led Blair et al. to suggest that photoionization of the unshocked ejecta plays an important role. Sutherland and Dopita (1995) included more elements and produced a grid of models for which they tabulated the emission from the

shocked gas and the precursor separately. They found that the precursor could make a very substantial contribution to the optical emission lines if the structure reaches a steady state between photoionizing flux and the flow of gas into the shock.

On the other hand, Blair et al. (2000) observed the O-rich remnants in the Magellanic Clouds N132D and 1E102-7219 with the FOS on HST, and they covered the 1200–8000 Årange. They found that a power law distribution of shock speeds within the FOS aperture could reproduce the UV to optical line ratios and the temperature-sensitive optical line ratios without a photoionization precursor, though a low temperature cutoff was still necessary to avoid overpredicting the lowest ionization lines. Because the knots are very small and subject to shearing and other instabilities when they encounter the reverse shock (Eriksen 2009), it is plausible and even probable that a range of shock speeds is present even within a small knot, and it is unlikely that a single steady-flow shock model is appropriate.

Part of the difficulty in assessing the importance of the precursor stems from the small size of the knots. The 10 year typical lifetime of knots in Cas A corresponds to a size smaller than 10^{16} cm, so the amount of photoionized, unshocked ejecta drops rapidly as the shock moves through the knot. For normal abundance SNR shocks, it is relatively easy to separate the emission from the pre- and post-shock gas. The pre-shock emission shows up as low surface brightness, diffuse emission ahead of the shock filaments in relatively nearby SNRs such as the Cygnus Loop (Szentgyorgyi et al. 2000; Medina et al. 2014), while in LMC SNRs it can show up as a narrow spectral feature at the rest velocity, distinct from the broad, Doppler-shifted emission from the shocked gas (Vancura et al. 1992). In the case of ejecta shocks, the spatial separation is tiny, and both pre- and post-shock gas are moving at thousands of km s^{-1}, while the pre- and post-shock velocities only differ by something like 100 km s^{-1}. A possible way to resolve the question is by comparing proper motions with the age of the remnant, since the shock decelerates the post-shock gas but not the precursor. In Cas A, explosion dates of 1662 ± 27 AD and 1672 ± 18 AD have been inferred from the positions and proper motions of all the outer ejecta knots and of a subsample of bright, compact knots, respectively (Fesen et al. 2006), while the SN might have been observed by the Reverend John Flamsteed in 1680. Taken at face value, the two proper motion dates would indicate decelerations, and therefore shock speeds, of 0.055 or 0.025 times the speeds of the knots, or about 150 to 550 km/s in the Cas A knots. In practice, the uncertainties in the explosion dates from proper motions are large enough to include the possible observation date, and the Flamsteed sighting is controversial (Stephenson and Green 2002).

6.2 Photoionized Precursors to Non-Radiative Shocks in Ejecta

Hamilton and Fesen (1988) studied the UV absorption line spectrum of the Schweizer-Middleditch star located behind the type Ia SNR SN1006. While it shows very strong Fe II absorption, the corresponding mass is much smaller than expected for a type Ia explosion. That led Hamilton and Fesen (1988) to investigate whether the unshocked ejecta could be photoionized to Fe III and above, which are not detectable in their wavelength range. While non-radiative shocks are inefficient in producing radiation, if they produced none at all they would be invisible. The photoabsorption cross sections at X-ray wavelengths are relatively small, but non-radiative shocks also produce UV emission as the elements are progressively ionized. Each ion below the ones found in equilibrium at T_e takes a time $1/(n_e q_i)$ to be ionized, where q_i is the ionization rate coefficient, typically a weak function of temperature for ions well below the ones that would be present at T_e. During that time, each spectral line of the ion is excited at a rate $n_e q_{ex}$, so each atom passing though the shock produces q_{ex}/q_i photons in the line. For strong permitted lines, that number is a few tens, while forbidden

lines have much smaller q_{ex} at high temperatures and the number is below one. Shocks in normal gas produce enough ionizing He I and He II photons to partially ionize the pre-shock gas (Morse et al. 1996; Ghavamian et al. 2000; Medina et al. 2014). Ejecta shocks produce quite a few ionizing photons per O atom, for instance, so they can produce many ionizing photons per atom passing through the shock.

Hamilton and Fesen (1988) computed the number of ionizing photons for the ions of O and Fe, and they found of order 1 to 10 ionizing UV photons for most ions. Putting those numbers into hydrodynamic simulations, they found that the unshocked Fe ejecta is mostly Fe IV and Fe V. Blair et al. (1996) observed the Schweizer-Middleditch star with the Hopkins Ultraviolet Telescope to search for the Fe III line at 1123 Å. Their 3σ upper limit corresponds to 0.054 M$_\odot$ of Fe III, which is consistent with the Hamilton and Fesen (1988) model. An additional process could enhance the photoionization rate beyond that predicted by Hamilton and Fesen (1988). Laming et al. (1996) found that in non-radiative shocks faster than about 1000 km s^{-1}, protons and alpha particles could excite UV emission lines as effectively as do electrons. This process, along with the related ionization rates, is sensitive to the threshold energy of the transition, and in the 1000 to 3000 km s^{-1} range, the protons could excite UV transitions around 10 eV, but they could not ionize the corresponding ions. Thus they increased the number of UV photons per atom passing through the shock. The excitation rates scale roughly as Z^2, while the number of electrons per ion is Z, so the ratio of ion to electron excitation increases as Z.

Another interesting case of photoionization of the unshocked ejecta is the recovered supernova S And, also known as SN 1885A in M31 (Fesen et al. 1999, 2015). It is seen in absorption against the bulge of M31 in lines of Ca I, Ca II, Fe I and Fe II, along with probable lines of Mg and other elements. The absorption lines show expansion velocities of 13,000 km/s and relative abundances consistent with a type Ia explosion. The ejecta are less ionized than those in SN1006, perhaps because of the small age of S And or because a low ambient density means that relatively little material has gone through the reverse shock thus far.

6.3 Photoionization by PWNe

The obvious case of photoionization by the synchrotron emission from a PWN is the Crab Nebula. The ejecta show high He, C and O abundances due to CNO processing, but not the more completely burned composition of the O-rich remnants discussed above (Sibley et al. 2016). While both shocked and unshocked ejecta are ionized, the gas that has been compressed by the shock driven by the expanding PWN has a much higher emissivity, and it produces the prominent filaments of the Crab (Sankrit and Hester 1997; Sankrit et al. 1998; Loll et al. 2013).

The Crab's optical emission lines are basically explained by photoionization of the compressed gas without any major contribution from the thermal energy of the shock, though the high temperature region behind the shock can contribute significantly to the UV lines because of their sensitivity to temperature. The radiative shock creates a dense shell that is accelerated by the PWN, leading to development of the Rayleigh-Taylor instability and the radial structures and strong clumping seen in some parts of the Crab (Hester et al. 1996; Loll et al. 2013). One characteristic of photoionization by the PWN power law emission is the simultaneous presence of high and low ionization emission from the outer and inner parts of the filaments, respectively. The cool cores of the filaments produce strong emission in low temperature lines, but not enough to account for the strong emission near 24 μm (Temim et al. 2006). The remnant 3C 58 may be similar, but has been less extensively studied (Fesen et al. 2008).

A case of a PWN inside O-rich SN ejecta is B0540-69.3 (Serafimovich et al. 2005; Morse et al. 2006; Williams et al. 2008). There, it appears that the pre-shock gas is photoionized to such an extent that a very slow shock shows relatively high ionization species and appears much like a faster shock (Williams et al. 2008), though faster shocks which might produce the observed emission without the assistance of photoionization by the PWN might also be present (Sandin et al. 2013). The young SNR G54.1+0.3 appears to be another case of shocks driven into the ejecta by the PWN, but the role of photoionization by the PWN is poorly constrained (Temim et al. 2010).
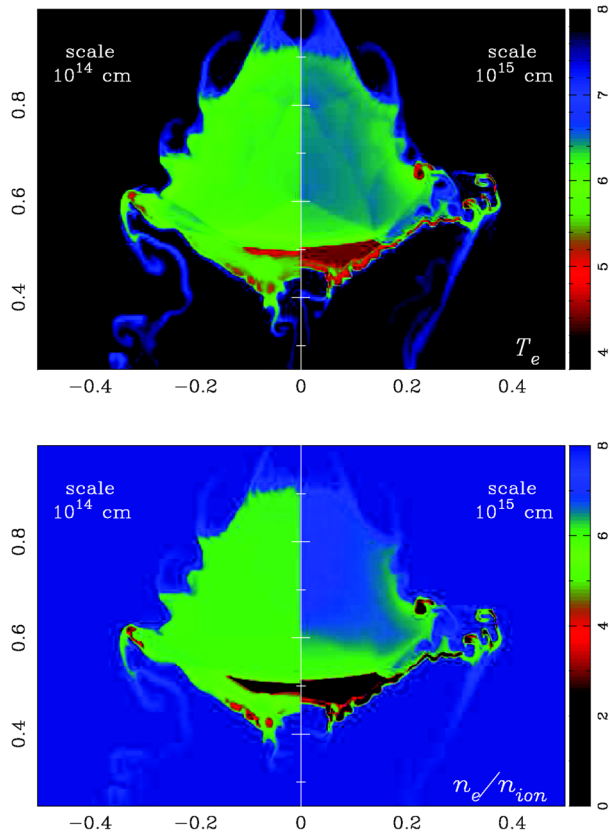
7 Instabilities

Radiative shock waves in SN ejecta are subject to the same instabilities that affect shocks in normal astrophysical plasma. Unless the cooling coefficient Λ increases rapidly with temperature, the shocks are thermally unstable (McCray et al. 1975; Chevalier and Imamura 1982; Innes et al. 1992; Innes 1992). Figure 1 indicates that shocks with electron temperatures above 10^6 K will be thermally unstable, and lower temperature shocks may be unstable depending upon the composition. The instability can be violent even in normal composition shocks, because the radiative cooling time can be shorter than the sound-crossing time in the cooling zone. That leads to extreme departures from pressure balance that cause the shock speed to oscillate. They also produce secondary shock waves that repressurize the gas to restore equilibrium. The enormous cooling rate of the shocked ejecta should exacerbate the departures from pressure equilibrium, though the time lag associated with the Coulomb collisional time scale for energy transfer from ions to electrons will limit the effect. Thermal conduction and non-thermal pressure from magnetic fields or cosmic rays may also limit the strengths of secondary shocks (Innes 1992). In any case it is likely that thermal instabilities play a major role in the discrepancies between observed spectra and planar, steady-flow models of shocks in O-rich SNRs.

Another important instability is the thin shell instability first studied by Vishniac (1983). Radiative cooling produces a thin, dense shell that is subject to the ram pressure of the upstream gas and thermal pressure of hot, low density gas in the SNR interior. When the shell is rippled, those forces are not aligned, and the ripples grow. The rapid cooling of shocks in the ejecta means that such shells are produced very quickly. However, the instability takes some time to develop, and if the ejecta are clumpy, as seems to be the case in the O-rich SNRs, the pre-shock density inhomogeneity may be a more important factor in the appearance of the radiative shocks.

Two other fluid instabilities are also important. Rayleigh-Taylor instabilities, or their shock analogue Richtmeyer-Meshkov instabilities, pertain to a dense fluid accelerated by a less dense one. The Rayleigh-Taylor instability at the contact discontinuity has been investigated for many years (Gull 1975; Blondin and Ellison 2001), and it can be even more severe when the ejecta are strongly clumped before they encounter the reverse shock. Either Rayleigh-Taylor fingers or pre-existing clumps form strong shear layers as they pass trough the surrounding gas, generating Kelvin-Helmholtz instabilities that shred the dense clumps and mix the plasmas of different density, temperature and composition. The process has been explored numerically for ordinary astrophysical plasmas (Klein et al. 1994; MacLow et al. 1994; Hansen et al. 2017), but the enormous cooling rates make it challenging to simulate for strongly enriched SN ejecta. Itoh (1988) appealed to turbulent stripping of dense knots to explain the lack of O I recombination lines in the optical spectrum, but the only numerical simulation is that of Eriksen (2009). Figure 9 shows a 2D model that assumes a spherical

Fig. 9 Simulations of two similar dense oxygen knots of 10^{14} and 10^{15} cm size passing through the reverse shock (Eriksen 2009). In this 2D model, the spherical cloud is 200 times denser than the surrounding medium. The *upper panel* gives $\log(T)$, and the *lower panel* gives the ionization state; for instance, $n_e/n_i = 6$ corresponds to O VII

cloud of pure oxygen gas with a density contrast of 200 and an incident shock of 2500 km/s. As in the normal abundance cases, the cloud rapidly develops a complex structure due to the fluid instabilities, and a wide range of ionization states is present, but the computer resources were insufficient to cover the large dynamic range of the problem.

8 Particle Acceleration

It is often assumed that particle acceleration at SNR reverse shocks is inefficient. First, the elemental abundances of cosmic rays (Cummings et al. 2016) are enhanced relative to protons, but not nearly to the extent observed in SN ejecta. Rather, the cosmic ray abundances look like ISM abundances modified by the charge-to-mass ratio effects expected from Diffusive Shock Acceleration with some further enhancement of species sputtered from dust grains (Drury 2001). Second, no X-ray synchrotron emission is generally seen from the reverse shock region. However, an inner ring of X-ray synchrotron radio emission is observed in Cas A (Gotthelf et al. 2001). Helder and Vink (2008) used Lucy-Richardson deconvolution to show that the inner X-ray ring arises from the region of the reverse shock, and it is not a projection of emission from a distorted blast wave. Also, the theoretical analysis by Zirakashvili et al. (2014) somewhat favors acceleration at the reverse shock in Cas A. One other SNR has been suggested as an example of X-ray synchrotron emission from the

reverse shock, RX J1713.7-3946 (Zirakashvili and Aharonian 2010), but the position of the reverse shock is not independently known and the interpretation is ambiguous.

Young type Ia SNRs such as Tycho and SN1006 show no evidence of X-ray synchrotron emission from the reverse shock in radio or X-rays, though Dickel et al. (1991) show that the radio emission from Tycho consists of a thin shell at the forward shock and a thicker shell in the region of the turbulent contact discontinuity between shocked ejecta and shocked ISM. Kosenko et al. (2011) found that acceleration at the reverse shock in Tycho must be less efficient than at the forward shock in order to match observations, while Schure et al. (2010) pointed out that particles accelerated at the forward shock could be re-accelerated at the reverse shock if the magnetic field there is sufficiently strong. Telezhinsky et al. (2012) construct models assuming a significant magnetic field at the reverse shock, and they find that acceleration at the reverse shock can affect the morphology, the spectrum and the evolution of synchrotron emission in type Ia SNRs. Telezhinsky et al. (2013) construct similar models for core-collapse SNRs.

To the extent that it is true that Cas A is fairly unique in showing strong synchrotron X-ray emission from the reverse shock, it is likely a result of the unusually strong perturbations of the reverse shock front due to the strong density inhomogeneities in the ejecta, both the large scale rings (Milisavljevic and Fesen 2015) and the small scale knots (Fesen et al. 2011). Either of these might amplify the magnetic field dramatically, but the small scale knots especially can generate strong small-scale vorticity that can amplify the field very rapidly. It is also possible that vorticity and magnetic fields were generated when the dense knots were first formed during the early stages of the explosion.

9 Abundance, Shock Speeds and Pressures in Shocks in Ejecta

The main applications of shock models for SN ejecta are to derive the elemental abundances for comparison with SN explosion models and to derive the shock parameters for comparison with dynamical models of the SNR evolution. Thus it is important to know how accurately the abundances, density and reverse shock speed can be estimated from observed spectra. We consider first non-radiative, then radiative shocks, which are equivalent to X-ray or to UV/optical/IR observations, respectively. It should also be remembered that the mass of unshocked ejecta can only be determined in a few cases; Cas A has about 0.4 $M_\odot$ (Isensee et al. 2010; DeLaney et al. 2014), SN1006 has about 0.04 $M_\odot$ of Fe and 0.25 $M_\odot$ of Si, with about half as much S and Si (Hamilton et al. 1997; Blair et al. 1996), and S And shows 0.1 to 1 $M_\odot$ of Fe (Fesen et al. 2015). There may also be a significant amount of mass locked up in dust, for instance 0.1 $M_\odot$ in Cas A (De Looze et al. 2017).

9.1 Parameters from X-Ray Spectra

As discussed in Sect. 4.1, a fast reverse shock provides some heat to the electrons (Yamaguchi et al. 2014), but Coulomb collisions soon dominate and bring kT_e to 1–3 keV. X-ray spectra are typically compared with models in which T_e is suddenly increased. The model parameters are T_e, the elemental abundances, and the ionization age, $n_e t$, which determines how far the plasma progresses toward ionization equilibrium. Smith and Hughes (2010) show the characteristic ionization age scales for different elements as functions of temperature. In effect, T_e is determined from the Boltzmann factor $e^{-h\nu/T}$ which enters most of the atomic processes that produce the X-ray spectrum, and $n_e t$ is determined by the ratios of different stages of ionization. To the extent that those numbers are accurate, the elemental

abundances should also be accurate. There are some caveats, however. An X-ray synchrotron contribution could affect the T_e estimate, and both T_e and $n_e t$ are averages over the observed volume. Problems might arise if $n_e t$ is different for different elements, as would be expected in a layered explosion.

The dynamical parameters also carry some uncertainty. It is easy to measure T_e from the X-ray spectrum, but very difficult to measure the ion temperature, and the relation between T_e and shock speed is model-dependent. The density estimate contains a factor of $f^{1/2}$, where f is the filling factor. The filling factor also affects estimates of the total ejecta mass.

A partial solution to both problems is increasing the spatial resolution of the observations, which often means increasing the exposure time in order to obtain enough counts in smaller resolution elements. Higher spectral resolution with instruments such as LYNX (http://adsabs.harvard.edu/abs/2016SPIE.9904E..0NG) and ATHENA (http://adsabs.harvard.edu/abs/2012SPIE.8443E..28R) will help by adding velocity information and helping to separate different contributions along the line of sight.

9.2 Parameters from UV/Optical/IR Spectra

As discussed above, there are substantial uncertainties in models of radiative shocks in highly enriched gas regarding electron-ion temperature equilibration and the effects of instabilities and density inhomogeneities on the emission spectra. One approach, if one has a spectrum covering a large wavelength range, is to add the spectra of shocks over a range of velocities, with the weighting chosen to match the relative intensities of lines from different ionization states. This especially makes sense if one is observing an extragalactic object, because the field of view is bound to include a range of shock parameters. Vancura et al. (1992) introduced this technique for the normal abundance SNR N49 in the LMC, and Blair et al. (2000) and France et al. (2009) applied it to the O-rich Magellanic Cloud remnants N132D and 1E102.2-7219.

Blair et al. (2000) were able to match the relative intensities of UV and optical lines of O I, O II, O III and O IV to establish the relative ionization states, along with the temperature-sensitive ratios of the O III lines $\lambda\lambda$1664, 4363, 5007. They then assumed that the model that matched the ionization state and temperature for O gave the correct set of temperature and ionization for the other elements to determine the abundances of C, Ne and Mg. This technique obviously works best if lines of several ionization states of the other elements are available. In this case Ne III, Ne IV and Ne V and C II, C III and C IV were observed, but the only observable ion of Mg was Mg II. Blair et al. (2000) concluded that the O:C ratios were 16 and 32 for 1E102 and N132D and the O:Ne ratios were 3.2 and 5.6, while the O:Mg ratios were 10–20 and 20–40, respectively. The match between models and observations was not perfect, of course, especially at the low (O I) and high (Ne V) ends, but the general agreement of the C II/C III and Ne III/Ne IV ratios with the models indicates that procedure works well for the dominant ion states and the abundance determinations are reliable.

The same cannot be said for the distribution of shock speeds used in the model itself. It is probable that instabilities and the shredding of dense knots lead to a much different distribution of temperatures than is given by a 1D shock model, and the assumed distribution of shock speeds is a way of mocking up that distribution. All one can say with confidence is that speeds of order 100 km/s are needed to produce the observed ionization states and temperatures.

If only a modest portion of the spectrum is available, it is difficult to observe more than 1 or 2 ionization stages for a given element. In that case if there are ions of 2 elements that have very similar ionization fractions and which have lines of similar excitation potential, the

abundance can be estimated from the atomic rates alone, without recourse of hydrodynamic models. The [P II] and [Fe II] lines in the near infrared present one example. The relative abundances of P and Fe were derived for dozens of knots in Cas A by Koo et al. (2013).

10 Shocks in Supernovae

The emission from most supernovae is powered by radioactive decay, but in some core-collapse SNe the interaction between the ejecta and a dense circumstellar medium (CSM) dominates. In type II-L and type IIn SNe, the ejecta come from the red supergiant envelope, and the abundances are fairly normal. In type Ib, the abundances resemble those of Wolf-Rayet stars.

As time goes on, the reverse shock caused by the interaction penetrates more and more deeply into the ejecta, and it eventually reaches the layers devoid of H. Late-time spectra sometimes show a progression, in which Hα fades and [O III] brightens, presumably due to the changing abundances (Milisavljevic et al. 2012). An example is SN 2014C, in which the spectrum evolved from type Ib to type IIn, with weak Hα absorption near maximum light. At later times, the SN developed strong Hα emission. The narrow line widths showed that the H and the highly ionized Fe emission originated in a photoionized circumstellar shell, while a component with an intermediate line width ($\sim$1200 km/s) may arise from shocked CSM material (Milisavljevic et al. 2015).

SN 1993J, like SN 2014C, showed weak Hα at early times, but it quickly evolved to type IIb. Over the course of a few years the [O III]/Hα ratio increased by an order of magnitude (Milisavljevic et al. 2012). X-ray studies by Nymark and Fransson (2009) and Chandra et al. (2009) found that most of the X-rays come from the reverse shock, that the lower temperature components are from radiative shocks, and that the X-ray spectrum indicates that the reverse shock was encountering gas that is N-rich and O-poor. The broad feature near Hα is likely to have a strong contribution from [N II] (Jerkstrand et al. 2015). Given that at least parts of the reverse shock are radiative, a partial dense shell will form. In SN 1993J, the density of the shell is expected to be above 10^{10} cm^{-3}, a density so high that forbidden lines are suppressed, and the [O III] I(4363)/I(5007) ratio would greatly exceed the observed upper limit if the [O III] were produced in the shell. Therefore, it seems that the [O III] comes from a photoionization precursor to the reverse shock of the sort discussed in Sect. 6.2. The [O III] luminosity is on the order of 10% of the X-ray luminosity, which suggests very efficient reprocessing of the EUV and X-ray radiation from the reverse shock.

Eventually, the reverse shock will encounter the layers devoid of H and He. If the density is still high and the shock is radiative, it might be observable in the UV if the reddening is not too severe. If oxygen dominates, the intercombination transitions of [O III] and [O IV] should be bright.

11 Summary

Shock waves in highly enriched SN ejecta differ from those in astrophysical plasma of normal abundances because of the enormous cooling rates. The rapid cooling can lead to extreme departures from electron-ion temperature equilibrium as well as collisional ionization equilibrium. It can also enhance fluid instabilities which disrupt simple 1D flows.

For the purposes of inferring elemental abundances, shock wave models that match the observed ratios of ionization states and the observed temperature-sensitive line ratios should

give reliable results. However, the uncertainty in electron-ion temperature ratios makes it difficult to infer shock speeds in either radiative or non-radiative shocks from optical/UV or X-ray spectra.

Appendix

For the reader's convenience, we list the SNRs showing shocks in O-rich material, along with some recent references that cite earlier works. The list of references is not intended to be complete or to include studies not directly related to shocks in enriched ejecta.

Cas A is the brightest and best known O-rich SNR. A comprehensive study of the X-ray spectra is given by Hwang and Laming (2012), and optical studies include Patnaude and Fesen (2014) and Milisavljevic and Fesen (2015). A near IR study is described by Koo et al. (2013) and mid-IR spectra by Isensee et al. (2010).

The bright O-rich SNR N132D is in the LMC. Schenck et al. (2016) analyze the X-ray spectrum, and France et al. (2009) analyze a UV spectrum from COS. Blair et al. (2000) discuss optical and UV spectra obtained with the FOS on HST. Tappe et al. (2012) obtained Spitzer spectra of N132D. They concentrate on PAH emission from the blast wave, but they also show a spectrum of the ejecta knots dominated by [Ne II] and [Ne III].

The SMC supernova remnant 1E102.2-7219 was observed in X-rays by Plucinsky et al. (2017) and Flanagan et al. (2004). The far UV spectrum was obtained by FUSE (Sasaki et al. 2006), and the rest of the UV spectrum is given by Blair et al. (2000). Blair et al. (2000) also give the optical spectrum, and Vogt et al. (2017) present an IFU study of the optical structure. Spitzer IR data are presented by Rho et al. (2009).

The LMC remnant B0540-69.3 is an O-rich remnant photoionized by a PWN. Brantseg et al. (2014) present the X-ray spectra, along with radio and optical images. Morse et al. (2006) give optical images and spectra from HST, and Williams et al. (2008) analyze the IR spectrum.

The X-ray spectrum of the very young O-rich SNR in NGC 4449 was analyzed by Patnaude and Fesen (2003), and its optical spectrum is given by Milisavljevic and Fesen (2010).

The Galactic SNR G292.0+1.8 has been observed in X-rays by Bhalerao et al. (2015) and Kamitsukasa et al. (2014), and in the optical by Winkler et al. (2009). Ghavamian et al. (2012) analyze Spitzer spectra and images.

The Puppis A supernova remnant is brightest in normal abundance material, but it contains a small region of shocked ejecta. Katsuda et al. (2010) give the X-ray spectrum and Winkler and Kirshner (1985) give the optical.

G54.1+0.3 is a PWN-dominated supernova remnant similar to B0540-69.3, except that no thermal X-ray emission is seen, and the IR spectrum is dominated by intermediate mass elements (Temim et al. 2010).

References

A. Bemporad, R. Susino, G. Lapenta, Astrophys. J. **784**, 102 (2014)
D. Berdichevsky, J. Giess, G. Gloeckler, U. Marshall, J. Geophys. Res. **102**, 2623 (1977)
J. Bhalerao, S. park, D. Dewey, J.P. Hughes, K. Mori, J.-J. Lee, Astrophys. J. **800**, 65 (2015)

W.P. Blair, J.C. Raymond, J. Danziger, F. Mateucci, Astrophys. J. **338**, 812 (1989)

W.P. Blair, J.C. Raymond, K.S. Long, Astrophys. J. **423**, 334 (1994)

W.P. Blair, K.S. Long, J.C. Raymond, Astrophys. J. **468**, 871 (1996)

W.P. Blair et al., Astrophys. J. **537**, 667 (2000)

J.M. Blondin, D.C. Ellison, Astrophys. J. **560**, 244 (2001)

K.J. Borkowski, J.M. Shull, Astrophys. J. **348**, 169 (1990)

T. Brantseg, R.L. McEntaffer, L.M. Bozzetto, M. Filipovic, N. Grieves, Astrophys. J. **780**, 50 (2014)

S. Broersen, J. Vink, Mon. Not. R. Astron. Soc. **446**, 3885 (2014)

S. Broersen, J. Vink, M. Miceli, F. Bocchino, G. Maurin, A. Decourchelle, Astron. Astrophys. **552**, 9 (2013)

A.M. Bykov, Y.A. Uvarov, J. Exp. Theor. Phys. **88**, 465 (1999)

A.M. Bykov, F.B.S. Paerels, V. Petrosian, Space Sci. Rev. **134**, 141 (2008)

P.J. Cargill, K. Papadopoulos, Astrophys. J. Lett. **329**, 29 (1988)

P. Chandra, V.V. Dwarkadas, A. Ray, S. Immler, D. Pooley, Astrophys. J. **699**, 388 (2009)

R.A. Chevalier, J.N. Imamura, Astrophys. J. **261**, 543 (1982)

R.A. Chevalier, J.C. Raymond, Astrophys. J. Lett. **225**, L27 (1978)

R.A. Chevalier, R.P. Kirshner, J.C. Raymond, Astrophys. J. **235**, 186 (1980)

A.C. Cummings et al., Astrophys. J. **831**, 18 (2016)

I. De Looze, M.J. Barlow, B.M. Swinyard, J. Rho, H.L. Gomez, M. Matsuura, R. Wesson, Mon. Not. R. Astron. Soc. **465**, 3309 (2017)

g. Del Zanna, K.P. Dere, P. Young, E. Landi, H.E. Mason, Astron. Astrophys. **582**, 56 (2015)

T. DeLaney, N.E. Kassim, L. Rudnick, R.A. Perley, Astrophys. J. **785**, 7 (2014)

J.R. Dickel, W.J.M. van Breugel, R.G. Strom, Astron. J. **101**, 2151 (1991)

M.A. Dopita, L. Binette, I.R. Tuohy, Astrophys. J. **282**, 142 (1984)

L.OC. Drury, Nature **99**, 329 (2001)

K.A. Eriksen Ph.D. thesis, University Arizona, 2009

R.A. Fesen, C.L. Gerardy, K.M. McLin, A.J.S. Hamilton, Astrophys. J. **514**, 195 (1999)

R.A. Fesen et al., Astrophys. J. **645**, 283 (2006)

R. Fesen, G. Rudie, A. Hurford, A. Soto, Astrophys. J. **174**, 379 (2008)

R.A. Fesen, J.A. Zastrow, M.C. Hammell, J.M. Shull, D.W. Silvia, Astrophys. J. **736**, 109 (2011)

R.A. Fesen, P.A. Höflich, A.J.S. Hamilton, Astrophys. J. **804**, 140 (2015)

K.A. Flanagan et al., Astrophys. J. **605**, 230 (2004)

K. France et al., Astrophys. J. Lett. **707**, L27 (2009)

T.J. Gaetz, R.J. Edgar, R.A. Chevalier, Astrophys. J. **329**, 927 (1988)

P. Ghavamian, J. Raymond, P. Hartigan, W.P. Blair, Astrophys. J. **535**, 266 (2000)

P. Ghavamian, J. Raymond, R.C. Smith, P. Hartigan, Astrophys. J. **547**, 995 (2001)

P. Ghavamian, P.F. Winkler, J.C. Raymond, K.S. Long, Astrophys. J. **572**, 888 (2002)

P. Ghavamian, J.M. Laming, C.E. Rakowski, Astrophys. J. Lett. **654**, 69 (2007a)

P. Ghavamian, W.P. Blair, R. Sankrit, J.C. Raymond, J.P. Hughes, Astrophys. J. **664**, 304 (2007b)

P. Ghavamian et al., Astrophys. J. **750**, 39 (2012)

P. Ghavamian, S.J. Schwartz, J. Mitchell, A. Masters, J.M. Laming, Space Sci. Rev. **47**, 557 (2013)

J. Giacalone, Space Sci. Rev. **176**, 73 (2013)

E.V. Gotthelf, B. Koralesky, L. Rudnick, T.W. Jones, U. Hwang, R. Petre, Astrophys. J. Lett. **522**, L39 (2001)

N. Grevesse, M. Asplund, A.J. Sauval, Space Sci. Rev. **130**, 105 (2007)

J. Grun, J. Stamper, C. Manka, R. Resnick, J. Crawford, B.H. Ripin, Phys. Rev. Lett. **66**, 2738 (1991)

S.F. Gull, Mon. Not. R. Astron. Soc. **171**, 263 (1975)

A.J.S. Hamilton, R.A. Fesen, Astrophys. J. **327**, 178 (1988)

A.J.S. Hamilton, R.A. Fesen, C.-C. Wu, D.M. Crenshaw, C.L. Sarazin, Astrophys. J. **481**, 838 (1997)

A.J.S. Hamilton, R.A. Fesen, W.P. Blair, Mon. Not. R. Astron. Soc. **381**, 771 (2007)

E.C. Hansen, A. Frank, P. Hartigan, S.V. lebedev, Astrophys. J. **837**, 143 (2017)

E.A. Helder, J. Vink, Astrophys. J. **686**, 1094 (2008)

E.A. Helder, J. Vink, C.G. Bassa, Astrophys. J. **737**, 85 (2011)

J.J. Hester, J.C. Raymond, W.P. Blair, Astrophys. J. **420**, 721 (1994)

J.J. Hester et al., Astrophys. J. **456**, 225 (1996)

L. Hovey, J.P. Hughes, K. Eriksen, Astrophys. J. **809**, 119 (2015)

J.P. Hughes, C.E. Rakowski, A. Decourchelle, Astrophys. J. Lett. **543**, 61 (2000)

A.J. Hull, J.D. Scudder, R.J. Fitzenreiter, K.W. Ogilvie, J.A. Newbury, C.T. Russell, J. Geophys. Res., Atmos. **105**, 20957 (2000)

U. Hwang, J.M. Laming, Astrophys. J. **746**, 130 (2012)

D.E. Innes, Astron. Astrophys. **256**, 660 (1992)

D.E. Innes, J.R. Giddings, S.A.E.G. Falle, Mon. Not. R. Astron. Soc. **224**, 179 (1992)

K. Isensee et al., Astrophys. J. **725**, 2059 (2010)

H. Itoh, Publ. Astron. Soc. Jpn. **29**, 813 (1977)

H. Itoh, Publ. Astron. Soc. Jpn. **30**, 489 (1978)

H. Itoh, Publ. Astron. Soc. Jpn. **33**, 1 (1981a)

H. Itoh, Publ. Astron. Soc. Jpn. **33**, 521 (1981b)

H. Itoh, Publ. Astron. Soc. Jpn. **38**, 717 (1986)

H. Itoh, Publ. Astron. Soc. Jpn. **40**, 673 (1988)

A. Jerkstrand, M. Ergon, S.J. Smartt et al., Astron. Astrophys. **573**, A12 (2015)

F. Kamitsukasa et al., Nature **66**, 64 (2014)

S. Katsuda, U. Hwang, R. Petre, S. Park, K. Mori, H. Tsunemi, Astrophys. J. **714**, 1725 (2010)

R.I. Klein, C.F. McKee, P. Colella, Astrophys. J. **420**, 213 (1994)

B.-C. Koo, Y.-H. Lee, D.-S. Moon, S.-C. Yoon, J.C. Raymond, Science **342**, 1346 (2013)

K.E. Korreck, J.C. Raymond, T.H. Zurbuchen, P. Ghavamian, Astrophys. J. **615**, 280 (2004)

K.E. Korreck, T.H. Zurbuchen, S.T. Lepri, J.M. Raines, Astrophys. J. **659**, 773 (2007)

D. Kosenko, J. Vink, S. Blinnikov, A. Rasmussen, Astron. Astrophys. **490**, 223 (2008)

D. Kosenko, S.I. Blinnikov, J. Vink, Astron. Astrophys. **532**, A114 (2011)

Yu.A. Kropotina, A.M. Bykov, M.Yu. Gustov, A.M. Krassilchtchikov, K.P. Levenfish, J. Tech. Phys. **60**, 231 (2015)

Yu.A. Kropotina, A.M. Bykov, A.M. Krassilchtchikov, K.P. Levenfish, J. Tech. Phys. **61**, 517 (2016)

J.W. Kruk, S.T. Durrance, G.A. Kriss, A.F. Davidson, W.P. Blair, B.R. Espey, D.S. Finley, Astrophys. J. Lett. **454**, L1 (1995)

J.M. Laming, J. Grun, Phys. Rev. Lett. **89**, 125002 (2002)

J.M. Laming, J.C. Raymond, B.M. McLaughlin, w.P. Blair, Astrophys. J. **472**, 267 (1996)

J.M. Laming, U. Hwang, P. Ghavamian, C. Rakowski, Astrophys. J. **790**, 11 (2014)

J.-J. Lee, B.-C. Koo, J.C. Raymond, P. Ghavamian, T.-S. Pyo, A. Tajitsu, M. Hayashi, Astrophys. J. Lett. **659**, L133 (2007)

J.-J. Lee, J.C. Raymond, S. Park, W.P. Blair, P. Ghavamian, P.F. Winkler, K. Korreck, Astrophys. J. Lett. **715**, 146 (2010)

A.M. Loll, S.J. Desch, P.A. Scowen, J.P. Foy, Astrophys. J. **765**, 152 (2013)

K.S. Long et al., Astrophys. J. **586**, 1162 (2003)

S. Ma et al., Astrophys. J. **738**, 160 (2011)

M.-M. MacLow, C.F. McKee, R.I. Klein, J.M. Stone, M. Norman, Astrophys. J. **433**, 757 (1994)

R. McCray, R.F. Stein, M. Kafatos, Astrophys. J. **196**, 565 (1975)

A. Medina, J.C. Raymond, R.J. Edgar, N. Caldwell, R.A. Fesen, D. Milisavljevic, Astrophys. J. **791**, 30 (2014)

E.R. Micelotta et al., Space Sci. Rev. (2017, submitted)

D. Milisavljevic, R.A. Fesen, Astrophys. J. **677**, 306 (2010)

D. Milisavljevic, R.A. Fesen, Science **347**, 526 (2015)

D. Milisavljevic, R.A. Fesen, R.A. Chevalier, R.P. Kirshner, P. Challis, M. Turatto, Astrophys. J. **751**, 25 (2012)

D. Milisavljevic et al., Astrophys. J. **815**, 120 (2015)

J.A. Morse et al., Astron. J. **112**, 509 (1996)

J.A. Morse, N. Smith, W.P. Blair, R.P. Kirshner, P.F. Winkler, J.P. Hughes, Astrophys. J. **644**, 188 (2006)

F.S. Mozer, D. Sundkvist, J. Geophys. Res. **118**, 5413 (2013)

T.K. Nymark, C. Fransson, Astron. Astrophys. **494**, 179 (2009)

Y. Ohira, Mon. Not. R. Astron. Soc. **440**, 514 (2014)

Y. Ohira, F. Takahara, Astrophys. J. Lett. **661**, L171 (2007)

D.J. Patnaude, R.A. Fesen, Astrophys. J. **587**, 221 (2003)

D.J. Patnaude, R.A. Fesen, Astrophys. J. **789**, 138 (2014)

P. Plucinsky et al., Astron. Astrophys. **597**, 83 (2017)

C.E. Rakowski, P. Ghavamian, J.P. Hughes, Astrophys. J. **590**, 846 (2003)

C.E. Rakowski, J.M. Laming, P. Ghavamian, Astrophys. J. **684**, 348 (2008)

J.C. Raymond, Astrophys. J. Suppl. Ser. **39**, 1 (1979)

J.C. Raymond, W.P. Blair, K.S. Long, Astrophys. J. Lett. **454**, L31 (1995)

J.C. Raymond, P.A. Isenberg, J.M. Laming, Astrophys. J. **682**, 408 (2008)

J.C. Raymond, P.F. Winkler, W.P. Blair, J.-J. Lee, S. Park, Astrophys. J. **712**, 901 (2010)

J.C. Raymond, R.J. Edgar, P. Ghavamian, W.P. Blair, Astrophys. J. **805**, 152 (2015)

J. Rho, W.T. reach, A. Tappe, U. Hwang, J.D. Slavin, T. Kozasa, L. Dunne, Astrophys. J. **700**, 579 (2009)

M.A. Riquelme, A. Spitkovsky, Astrophys. J. **733**(1), 63 (2011). https://doi.org/10.1088/0004-637X/733/1/63

G. Salvesen, J.C. Raymond, R.J. Edgar, Astrophys. J. **702**, 327 (2009)

C. Sandin, P. Lundqvist, N. Lundqvist, C.-I. Björnsson, G. Olofsson, Yu.A. shibanov, Mon. Not. R. Astron. Soc. **432**, 2854 (2013)

R. Sankrit, J.J. Hester, Astrophys. J. **491**, 796 (1997)

R. Sankrit et al., Astrophys. J. **504**, 344 (1998)

A. Sarangi et al., Space Sci. Rev. (2017, submitted)

M. Sasaki, T.J. Gaetz, W.P. Blair, R.J. Edgar, J.A. Morse, P.P. Plucinsky, R.K. Smith, Astrophys. J. **642**, 260 (2006)

A. Schenck, S. Park, S. Post, Astrophys. J. **151**, 161 (2016)

K.M. Schure, A. Achterberg, R. Keppens, J. Vink, Mon. Not. R. Astron. Soc. **406**, 2633 (2010)

S.J. Schwartz, J. Geophys. Res. **119**, 1507 (2014)

S.J. Schwartz, M.F. Thomsen, S.J. Bame, J. Stansberry, J. Geophys. Res. **93**, 12923 (1988)

N.I. Serafimovich, P. Lundqvist, A. Shibanov Yu, J. Sollerman, Adv. Space Res. **35**, 1106 (2005)

N. Shimada, M. Hoshino, Astrophys. J. Lett. **543**, L71 (2000)

A.R. Sibley, A.M. Katz, T.J. Satterfield, S.J. Vanderveer, G.M. MacAlpine, Astron. J. **152**, 93 (2016)

R.C. Smith Ph.D. thesis, Harvard University, 1991

R.K. Smith, J.P. Hughes, Astrophys. J. **718**, 583 (2010)

R.C. Smith, J.C. Raymond, J.M. Laming, Astrophys. J. **420**, 286 (1994)

J. Sollerman, P. Ghavamian, P. Lundqvist, R.C. Smith, Astron. Astrophys. **407**, 249 (2003)

F.R. Stephenson, D.A. Green, in *Historical Supernovae and Their Remnants* (Clarendon, Oxford, 2002)

R.S. Sutherland, M.A. Dopita, Astrophys. J. **439**, 381 (1995)

F. Suzuki-Vidal et al., Astrophys. J. **815**, 96 (2015)

A.H. Szentgyorgyi, J.C. Raymond, J.J. Hester, S. Curiel, Astrophys. J. **529**, 279 (2000)

A. Tappe, J. Rho, C. Boersma, E.R. Micelotta, Astrophys. J. **754**, 132 (2012)

I. Telezhinsky, V.V. Dwarkadas, M. Pohl, Astropart. Phys. **35**, 300 (2012)

I. Telezhinsky, V.V. Dwarkadas, M. Pohl, Astron. Astrophys. **552**, 102 (2013)

T. Temim et al., Astron. J. **132**, 1610 (2006)

T. Temim, P. Slane, S.P. Reynolds, J.C. Raymond, K.J. Borkowski, Astrophys. J. **710**, 309 (2010)

O. Vancura, W.P. Blair, K.S. Long, J.C. Raymond, Astrophys. J. **394**, 158 (1992)

J. Vink, J.M. Laming, F.M. Gu, A. Rasmussen, J. Kaastra, Astrophys. J. Lett. **587**, L31 (2003)

J. Vink, S. Broersen, A. Bykov, S. Gabici, Astron. Astrophys. **579**, 13 (2015)

E.T. Vishniac, Astrophys. J. **274**, 152 (1983)

F.P.A. Vogt, I. Seitenzahl, M.A. Dopita, A.J. Ruiter, Publ. Astron. Soc. Pac. **129**, 058012 (2017)

L.L. Williams, G.P. Zank, J. Geophys. Res. **99**, 19229 (1994)

B.J. Williams et al., Astrophys. J. **687**, 1054 (2008)

P.F. Winkler, R.P. Kirshner, Astrophys. J. **299**, 981 (1985)

P.F. Winkler, K. Twelker, C.N. Reith, K.S. Long, Astrophys. J. **692**, 1489 (2009)

H. Yamaguchi, K. Eriksen, C. Badenes, J.O. Hughes, N. Brickhouse, A. Foster, D.J. Patnaude, R. Petre, P.O. Slane, R.K. Smith, Astrophys. J. **780**, 136 (2014)

G. Zimbardo, Planet. Space Sci. **59**, 468 (2011)

V.N. Zirakashvili, F.A. Aharonian, Astrophys. J. **708**, 965 (2010)

V.N. Zirakashvili, F.A. Aharonian, R. Yang, E. Oña-Wilhelmi, R.J. Tuffs, Astrophys. J. **785**, 130 (2014)